Journal of *Marine Science and Engineering*

MDPI

Article

Hydrodynamic Performance of an Oscillating Water Column Device Installed in an Offshore Wind Turbine

Chuanli Xu [1], Lei Ding [1], Yuting Sun [2] and Zhen Liu [1,3,4,*]

[1] Shandong Provincial Key Laboratory of Ocean Engineering, Ocean University of China, Qingdao 266100, China
[2] School of Hydraulic Engineering, Wanjiang University of Technology, Ma'anshan 243000, China
[3] Qingdao Municipal Key Laboratory of Ocean Renewable Energy, Ocean University of China, Qingdao 266100, China
[4] Center for Ocean Carbon Neutrality, Ocean University of China, Qingdao 266100, China
* Correspondence: liuzhen@ouc.edu.cn; Tel.: +86-532-6089-5309

Abstract: Hybrid wind–wave energy devices have attracted significant attention for their potential to efficiently harness marine energy while reducing construction costs. In this work, the hydrodynamic performance of an oscillating water column (OWC) device installed in an offshore wind turbine was investigated. A three-dimensional numerical model was developed based on computational fluid dynamics. The numerical predictions demonstrate good agreement with the corresponding experimental results. The effects of key factors, such as chamber diameter, chamber draft, and pneumatic damping, on the energy capture performance were analyzed. The variation patterns of the free surface elevation, the air pressure, and the capture width ratio were analyzed. Additionally, flow characteristics and vortex dynamics around the device were presented for better understanding the energy capture process of the hybrid device. The results reveal that a larger chamber diameter is beneficial for energy conversion, and the optimal chamber draft and pneumatic damping were identified. Furthermore, the operating performance of the optimized device under irregular wave conditions was predicted.

Keywords: wave energy; offshore wind turbine; hybrid device; numerical study; performance optimization

Academic Editor: Eva Loukogeorgaki

Received: 31 December 2024
Revised: 12 January 2025
Accepted: 16 January 2025
Published: 18 January 2025

Citation: Xu, C.; Ding, L.; Sun, Y.; Liu, Z. Hydrodynamic Performance of an Oscillating Water Column Device Installed in an Offshore Wind Turbine. *J. Mar. Sci. Eng.* **2025**, *13*, 169. https://doi.org/10.3390/jmse13010169

1. Introduction

Marine renewable energy is playing an increasingly significant role in ecological conservation and the development of low-carbon economies. Wave energy, characterized by its global distribution, abundant reserves, and ease of utilization, is currently the most widely applied and promising form of marine energy [1]. Based on energy conversion principles, wave energy systems can be categorized into oscillating water column (OWC), overtopping, and oscillating body types [2]. The OWC device features a simple structure, excellent corrosion resistance, and ease of maintenance. The overtopping device can convert unstable wave energy into stable potential energy of the water, enabling a steady and continuous energy output. The key characteristic of the oscillating body device is that the moving body is in direct contact with the waves, enabling more efficient conversion of wave energy into mechanical energy. Due to the immaturity of the technology, wave energy devices still face high levelized costs of electricity (LCOEs), thus hindering full commercialization. Among these technologies, OWC devices stand out for their simplicity and reliability: the only moving part, the air turbine, is located above the water, making it

resistant to corrosion and easy to maintain [3]. Several demonstration plants, such as the Mutriku plant, Yongsoo OWC, and OE Buoy, have already been successfully operating [4,5], showcasing the great feasibility and potential of OWC technology.

To harness more wave energy, researchers have optimized the conversion performance of OWC devices through experimental and numerical studies. Elhanafi and Kim [6] investigated the performance of a 3D offshore OWC device in experiments and found that the device achieved a higher capture width ratio under long waves with low-power take-off (PTO) damping. Kharati and Fathi [7] compared the effects of various chamber lengths and bottom slope angles on the efficiency of an OWC device. The device reached optimal efficiency with a low chamber length and a high bottom slope angle. Yamac and Koca [8] developed a computational fluid dynamics (CFD) numerical model for an OWC device and compared the effects of coastal structures on its output power. The results indicated that the OWC exhibited the best performance when the coast had a convex arc geometry. Trivedi et al. [9] studied the performance of the LIMPET OWC and analyzed the impact of energy dissipation on the hydrodynamic performance by presenting velocity vectors and streamlines during the fluctuation cycle. He et al. [10] employed the particle image velocimetry technique to report the flow field characteristics around an OWC device, exploring the relationship between energy dissipation and vortex formation. Mayon et al. [11] proposed an OWC system incorporating a cylindrical OWC and a parabolic wave reflector. This novel design significantly enhanced the energy capture efficiency and bandwidth of the device. Wang et al. [12] established a numerical model of a dual-chamber OWC with a pitching mid-wall and investigated the effects of the chamber breadth, mid-wall position, and draft on the device performance. M'zoughi et al. [13] presented an airflow control method for OWCs based on artificial neural networks. The control strategy demonstrated good performance and prevented the stalling behavior of the turbine. Liu et al. [14] proposed a novel speed-amplified flux switching linear generator and improved the conversion efficiency of the wave energy converter by 13.4% [14]. Compared to single-chamber OWCs, multiple-chamber OWCs demonstrate higher pneumatic efficiency due to reduced internal fluid sloshing [15]. Wang et al. [16] analyzed the differences between a five-unit OWC array and individual devices, finding that transverse spacing between units helps to mitigate destructive interactions and improves conversion performance.

In order to enhance commercial competitiveness, wave energy devices can be developed in combination with offshore structures such as marine platforms and breakwaters, which can help to reduce construction costs [17,18]. Naty et al. [19] studied the feasibility of installing wave energy devices within breakwaters. The optimized configuration reduced the reflection coefficient of the breakwater and enhanced its capture efficiency. Das et al. [20] proposed a novel concept of coupling an OWC device integrated with an overtopping device in breakwaters and evaluated the feasibility of its implementation in harbors. Xu and Huang [21] experimentally investigated the hydrodynamic characteristics of an OWC device coupled with pile breakwaters, finding that this configuration is beneficial for structural safety and coastal protection. Howe and Nader [22] compared the conversion performance of an OWC device when installed independently and when integrated with breakwaters. Ashlin et al. [23] tested the performance of array OWCs integrated with offshore detached breakwaters and found that the optimal performance is achieved when the spacing between the units is three times the model width. Zhao et al. [24] examined hydrodynamic coefficients for multi-chamber OWC breakwaters and concluded that the triple-chamber system performs better than conventional pontoon breakwaters. Zheng et al. [25,26] combined OWC devices with coastal structures and improved the hydrodynamic efficiency by optimizing the air chamber radius, wall thickness, and submergence. Vipin et al. [27] investigated the performance of a breakwater-integrated OWC device

in irregular waves. The parameters of the device were optimized by using a multilayer perceptron model and tree ensemble model. Wave energy devices can also be integrated with floating breakwaters, where this coupling not only enhances wave energy extraction but also contributes to the stability of the floating structure [28,29].

In recent years, hybrid wind–wave energy systems have gained attention due to their potential to fully utilize marine energy and share infrastructure, electrical equipment, and cabling costs [30]. Sarmiento et al. [31] coupled a floating semisubmersible structure with three OWC units and investigated the impact of different chamber opening configurations on platform response. Abbaspour and Farshforoush [32] introduced a hybrid energy harvesting platform combining a wind turbine with an OWC platform, finding that the total wave energy collection output increased sixteen times compared to isolated units. Lee et al. [33] numerically studied the performance of OWC devices integrated with jacket-type infrastructures for wind turbines and analyzed the effects of the geometrical parameters on the pneumatic power. Michele et al. [34] developed a numerical model based on linearized theory for an OWC-integrated wind turbine system. The effects of the skirt and internal radius dimensions on wave energy conversion were studied. Using linear potential flow theory, Zhou et al. [35] established a time-domain model for an OWC integrated into an offshore wind turbine monopole. The results showed that the introduction of the OWC reduced the horizontal and overturning moments on the monopile, thus enhancing the stability of the foundation structure. Cong et al. [36] coupled four OWC sub-chambers into a monopile wind turbine and found that the wave forces acting on the OWC and the monopile can balance each other under certain wave conditions.

From the literature review, integrating OWC devices with offshore wind turbines has emerged as a key direction in wave energy development. However, most of the previous studies have primarily focused on the effects of OWC dimensions on energy output and structural loads. The flow characteristics and vortex development at critical locations between the air chamber and the wind turbine foundation, which are crucial for understanding the energy capture mechanisms of hybrid wind–wave systems, remain to be further investigated. In this study, a numerical model of an OWC installed in a monopile foundation for an offshore wind turbine is developed based on CFD tools. The numerical results are validated by corresponding experimental tests. The effects of wave period, chamber diameter, chamber draft, and PTO damping on energy harvesting performance are analyzed. The flow characteristics around the key component are described. The main contribution of this work is to provide a deeper understanding of the energy capture process of the hybrid system, which will be helpful in optimizing the design of the device.

The rest of the paper is organized as follows. Section 2 illustrates the experimental setup and the numerical model. Section 3 presents the convergence analysis and the validation of the numerical model. The effects of the key parameters and wave conditions on the hydrodynamic behavior of the hybrid system are discussed in Section 4. Finally, the conclusions are summarized in Section 5.

2. Experimental and Numerical Setup

2.1. Experimental Model Setup

In order to investigate the fundamental hydrodynamic performance of the hybrid wind–wave device and to provide data for numerical validation, a model-scale device with a scale ratio of 1:10 following the Froude similarity law was designed and conducted. The hybrid OWC–wind model is illustrated in Figure 1. The internal cylinder represents a typical monopile foundation of an offshore wind turbine, with a cylindrical OWC chamber installed coaxially around the monopole, resulting in an annular cross-sectional shape of the water column. The air chamber is constructed from a 5 mm thick transparent acrylic

tube, facilitating the clear observation of free surface variations inside the chamber. The monopile has a diameter of l_1 = 0.3 m, and its total height is truncated to 1.35 m. The diameter and height of the air chamber are l_2 = 0.6 m and h_2 = 0.4 m, respectively. The bottom of the air chamber is set to be h_3 = 0.55 m above the ground. To simulate the PTO damping of an impulse air turbine, a circular orifice with a diameter of Φ = 0.052 m is located at the top of the chamber. The ratio of the orifice area to the water column area is α = 1%, and the effect of PTO damping on the hydrodynamic performance of the device will be examined in the subsequent section. Four capacitance-type wave gauges, with a measurement range of 700 mm and an accuracy of ±0.5% of full scope (FS), were arranged around the center of the chamber to monitor the variations in free surface. A pressure differential sensor with a measurement range of 1 kPa and an accuracy of ±0.5% (FS) was installed at the top of the chamber via a flexible tube to measure the air pressure variations.

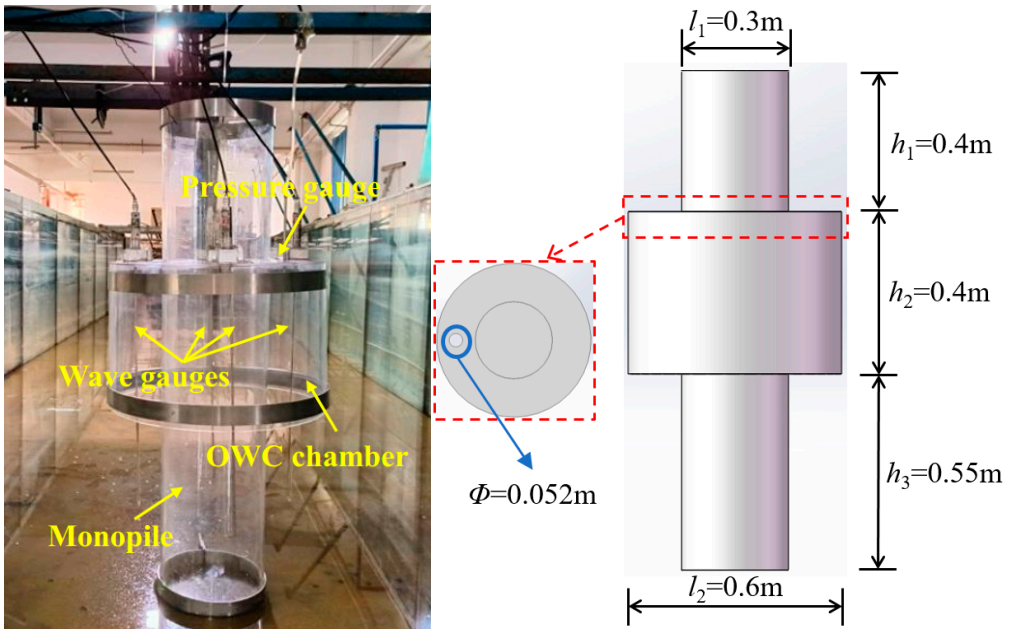

Figure 1. Depictions of the hybrid OWC–wind model. (**a**) Photo of the model; (**b**) model design.

The experimental tests were carried out in a wave flume at the Shandong Provincial Key Laboratory of Ocean Engineering. The wave flume has a length of 60.0 m, width of 3.0 m, and height of 1.5 m. A piston-type wave maker is installed at one end of the flume and is controlled by a servo motor, enabling it to move back and forth and generate both regular and irregular waves within a certain range. A porous media wave absorber is set at the opposite end to minimize wave reflection and is capable of absorbing most incident waves. The layout of the hybrid OWC–wind model is depicted in Figure 2. The model was fixed at the center of the flume with a distance of 35.0 m from the wave maker to ensure the sufficient development of the incident waves. The water depth and chamber draft were h = 0.75 m and d = 0.2 m, respectively. One regular incident wave height (H = 0.1 m) with four wave periods (T = 1.27 s, 1.45 s, 1.63 s, and 1.83 s) were selected. The dimensionless wave period λ/l_1 was considered, where λ represents the wave length corresponding to the wave period, with values of λ/l_1 = 8.0, 10.0, 12.0, and 14.0. All data were synchronously collected and processed using a data acquisition system. The tests were repeated three times, with the error between each result being less than 5%, and the average value was taken as the final result.

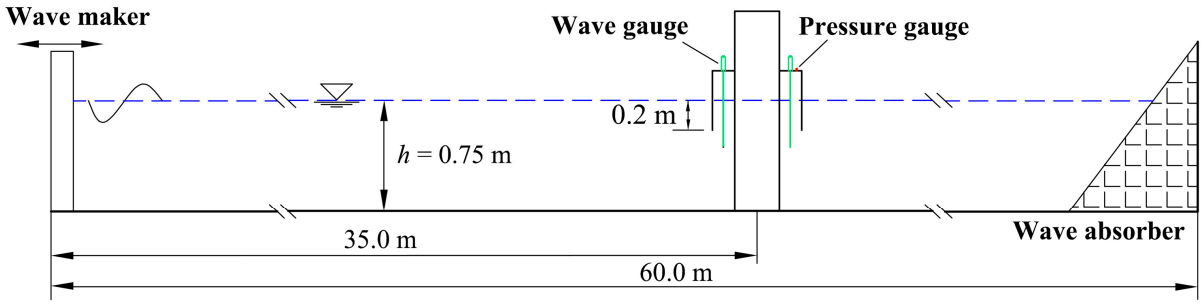

Figure 2. Layout of the experimental test.

The hydrodynamic performance of the OWC can be characterized by the capture width ratio (*CWR*), which can be calculated based on the following equations:

$$CWR = P_P / P_W \tag{1}$$

where P_P and P_W are the pneumatic power output of the OWC and the incident wave power, defined as

$$P_P = \frac{1}{nT}\int_0^{nT} p(t)\cdot Q(t)dt \tag{2}$$

$$P_W = \frac{1}{8}\rho g H^2 C_g l_2 \tag{3}$$

where $p(t)$ and $Q(t)$ are the instantaneous air pressure and air flow rate inside the chamber; n is the number of wave cycles; ρ, g, and C_g represent the water density, the gravitational acceleration, and the wave velocity, respectively.

2.2. Numerical Model Setup

To complement the experimental results and gain deeper insights into the flow characteristics, a numerical model of the hybrid OWC–wind device was developed using the CFD software ANSYS-Fluent 16.0. The numerical setup and the mesh structures are illustrated in Figure 3. In this model, since the waves do not overtop the air chamber and interact with the monopile, the internal cylinder above the OWC chamber was omitted to simplify the calculations. Apart from this, the dimensions of the numerical model remained fully consistent with those used in the experiment. As shown in Figure 3, structured grids were used in the regions near the two sides of the wave flume. The mesh size in length was maintained at less than one-fiftieth the minimum wave length, while the meshes near the free surface were refined to enhance the accuracy of fluid motion capture [37]. For the hybrid device domain, unstructured grids were employed and interface boundary conditions were applied to connect the different computational domains. In addition, except for the top of the wave flume, which was set as the pressure outlet boundary, all other boundary conditions were set as no-slip walls. A user-defined function (UDF) was employed to control the motion of the wave-making plate for wave generation. The velocity of the wave-making plate v can be written as

$$v(t) = \frac{S\cdot\omega}{2}\cos(\omega t) \tag{4}$$

where S and ω are the stroke and angular frequency of the wave-making plate, respectively. The stroke corresponding to each wave condition has been calibrated. A damping zone based on the source-term method was placed at the end of the flume for wave absorbing.

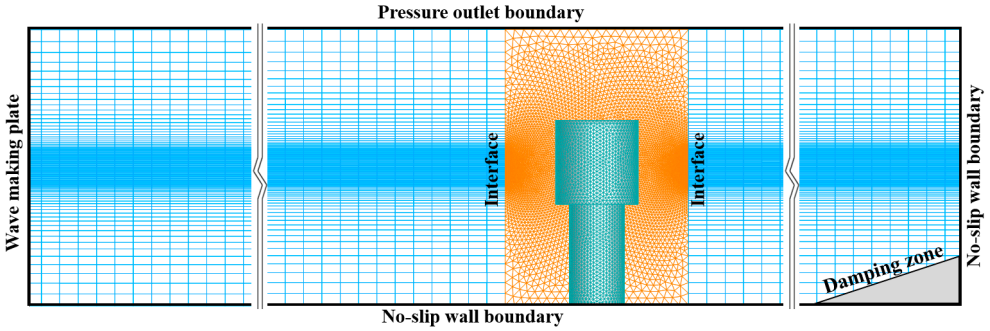

Figure 3. Computational domains and mesh structures of the numerical model.

The governing equations of the numerical model were based on the continuity equation and the Reynolds-averaged Navier–Stokes (RANS) equation, which can be described as follows:

$$\frac{\partial \rho}{\partial t} + \frac{\partial (\rho u_i)}{\partial x_i} = 0 \tag{5}$$

$$\frac{\partial u_i}{\partial t} + u_j \frac{\partial u_i}{\partial x_j} = -\frac{1}{\rho}\frac{\partial p}{\partial x_i} + g_i + \frac{1}{\rho}\frac{\partial \tau_{ij}}{\partial x_j} \tag{6}$$

where u_i represents the velocity components in each direction. i, j = 1, 2, 3 for 3D flow, g_i is ith component of the gravitational acceleration, and τ_{ij} is the viscous stress tensor [38]. In this model, the Reynolds stress terms were closed using the renormalization-group (RNG) k-ε turbulence model, which can effectively describe the turbulence and improve computational accuracy. The two-equation turbulence model can be written as follows:

$$\frac{\partial (\rho k)}{\partial t} + \frac{\partial (\rho k u_i)}{\partial x_i} = \frac{\partial}{\partial x_j}\left[\alpha_k (\mu + \mu_t)\frac{\partial k}{\partial x_j}\right] + G_k - \rho\varepsilon \tag{7}$$

$$\frac{\partial (\rho \varepsilon)}{\partial t} + \frac{\partial (\rho \varepsilon u_i)}{\partial x_i} = \frac{\partial}{\partial x_j}\left[\alpha_\varepsilon (\mu + \mu_t)\frac{\partial \varepsilon}{\partial x_j}\right] + \frac{\varepsilon}{k}(C_{1\varepsilon} G_k - C_{2\varepsilon}\rho\varepsilon) \tag{8}$$

where k and ε are the turbulence kinetic energy and the turbulent dissipation rate, respectively. α_k and α_ε are the inverse effective Prandtl numbers for k and ε, μ is the kinetic viscosity, and G_k is the turbulence kinetic energy induced by the mean velocity gradients. $C_{1\varepsilon}$ and $C_{2\varepsilon}$ are constants, with values of 1.42 and 1.68, respectively [39]. Due to the strong interaction between air and water in the OWC device, the volume of fluid (VOF) two-phase flow model was used to track the free surface. The numerical solution was obtained using the finite volume method. The pressure–velocity coupling was handled by the pressure implicit with splitting of operators (PISO) algorithm. For spatial discretization, the gradient interpolation was performed using the green-gauss cell-based method, and the pressure interpolation was carried out with the body-force-weighted method. The momentum terms were discretized using the second-order upwind scheme, and the transient terms were solved using the second-order implicit scheme. The above method for modeling the OWC had been verified in a previous study [40].

3. Validation of Numerical Results

3.1. Convergence Study

To ensure modeling accuracy and reduce computational cost, it is necessary to perform convergence verifications for the mesh size and time step of the numerical model. It has been demonstrated that, once the mesh reaches a certain number, the improvement in accuracy becomes negligible, while the computational time increases significantly. The

case with a wave height H = 0.1 m and wave period of T = 1.63 s was selected for verification. Figure 4a,b present the mesh convergence study for the free surface elevation and air pressure inside the air chamber. Three different sizes of mesh refinement zones were set, with the mesh sizes in the vertical direction corresponding to 1/5, 1/10, and 1/20 of the wave height. The corresponding numbers of mesh cells were $N = 3.8 \times 10^5$, 6.1×10^5, and 8.7×10^5, respectively. The time step was set as Δt = 0.0025 s. As shown in Figure 4, the relative free surface elevation a_I/A (where a_I and A represent the instantaneous elevation inside the chamber and the incident wave amplitude, respectively) and air pressure variations p for $N = 3.8 \times 10^5$ are much lower than for the other parameters, and the amplitude differences for these two parameters compared to $N = 8.7 \times 10^5$ are 7.5% and 9.3%, respectively. For $N = 6.1 \times 10^5$, the differences are 1.3% and 1.6% when compared to $N = 8.7 \times 10^5$, but the computational time was reduced to 64%. Therefore, a mesh number of $N = 6.1 \times 10^5$ was chosen for the subsequent calculations.

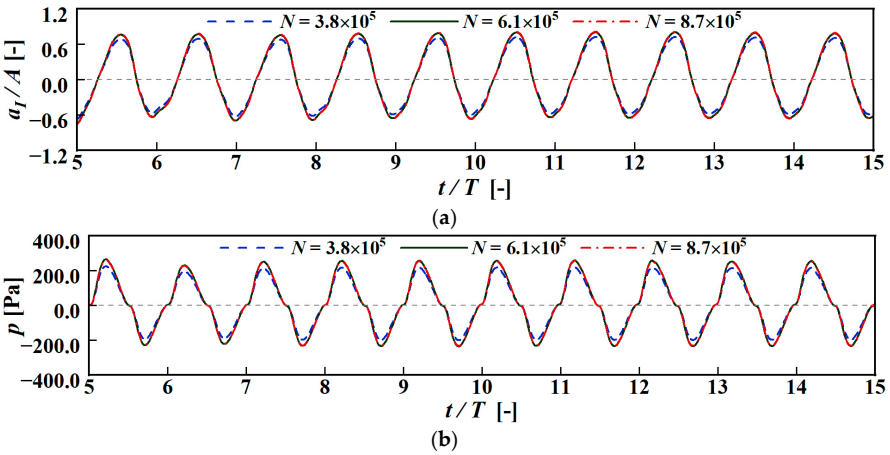

Figure 4. Convergence study of the mesh number. (**a**) Free surface elevation; (**b**) air pressure.

The convergence study of the computational time step is shown in Figure 5. Three different time steps were compared: Δt = 0.01 s, Δt = 0.005 s, and Δt = 0.0025 s, all of which are smaller than 1/100 of the wave period. The amplitude differences in free surface elevation and air pressure between Δt = 0.01 s and Δt = 0.0025 s are 15.3% and 24.2%, respectively. When the time step was reduced to Δt = 0.005 s, the differences compared to the smallest time step are only 2.1% and 3.2%, respectively. This indicates that the hydrodynamic results converge with a time step of Δt = 0.005 s. Therefore, this time step was set for the calculations.

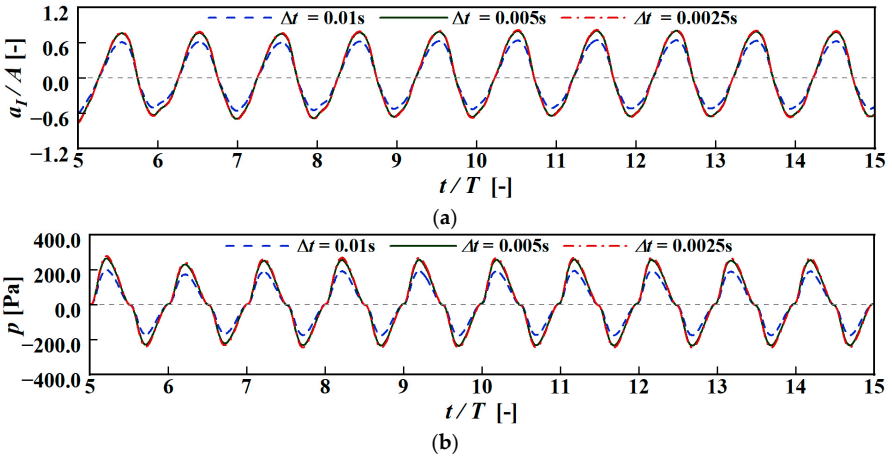

Figure 5. Convergence study of the time step. (**a**) Free surface elevation; (**b**) air pressure.

3.2. Comparison Between Experimental and Numerical Results

The hydrodynamic performance of the hybrid OWC–wind device is demonstrated and compared in Figure 6. As is evident from Figure 6a, the relative amplitude of the free surface elevation a/A (where a represents the average elevation amplitude) increases as the incident wave length increases, indicating that long-period waves are more likely to enter the chamber and induce oscillations. Additionally, the numerical results closely match the experimental results, with an average error of 3.1% across the different conditions. Figure 6b presents the dimensionless air pressure amplitudes inside the chamber, where $P^* = P/\rho gA$ and P represent the average pressure amplitude. Both the experimental and numerical results demonstrate similar trends, with an average error of 4.4%.

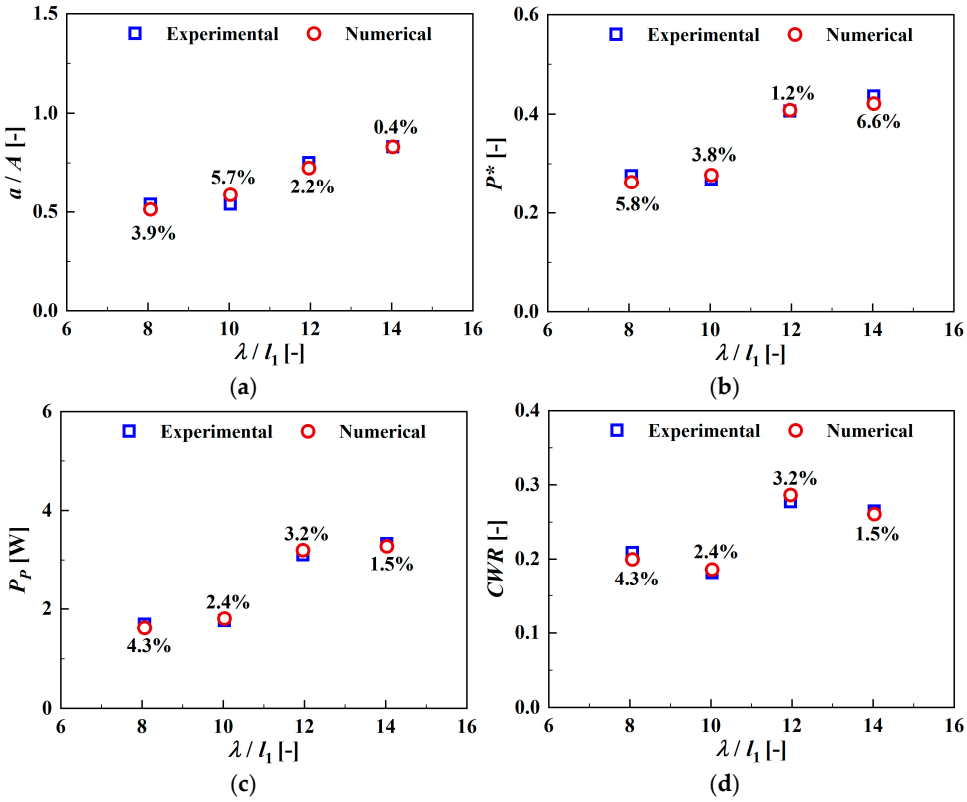

Figure 6. Comparison of experimental and numerical results. (**a**) Relative amplitude of free surface elevation; (**b**) relative amplitude of air pressure; (**c**) pneumatic power output; (**d**) capture width ratios.

The pneumatic power output of the OWC is depicted in Figure 6c. As the wave energy increases with the incident wave period, both the predicted results illustrate that the power output increases with the incident wave length. The average error between the numerical and experimental results is 2.9%. Figure 6d shows the results of the capture width ratio. Similar to the isolated OWC device [37], an optimal incident wave period can be observed at which the performance of the hybrid OWC–wind device is maximized. This behavior is associated with a strong resonance effect between the device and the incident waves. Compared with the experiments, the numerical model predicts the CWR with an average error of 2.9%. Overall, the numerical model is capable of accurately predicting the key hydrodynamic performance of the hybrid OWC–wind device and can be used for further simulations.

4. Results and Discussion

In this section, the flow characteristics of the hybrid OWC–wind device during the energy capture process are analyzed. The effects of key geometrical parameters including

the OWC chamber diameter, chamber draft, and PTO damping on the hydrodynamic performance are discussed. In addition, the operating performance under irregular waves, which more accurately represent real sea states, is evaluated.

4.1. Effect of Chamber Diameter

Diameter is a significant factor in determining the performance of a cylindrical OWC. In this section, five different OWC chamber diameters are considered, i.e., l_2 = 0.45 m, 0.525 m, 0.6 m, 0.75 m, and 0.9 m. The dimensionless ratio of the chamber diameter to the monopile diameter l_2/l_1 with values of 1.5, 1.75, 2.0, 2.5, and 3.0 are used for comparison. The dimensionless chamber draft and PTO damping are fixed at d/h = 0.15 and α = 1%, respectively.

The flow characteristics and vortex development at specific locations of the hybrid OWC–wind device during a wave cycle are depicted in Figure 7. The typical case of H = 0.1m, λ/l_1 = 12.0, and l_2/l_1 = 2.0 is selected, and the wave direction is from left to right. At the moment of $T/4$ in Figure 7a, the OWC device reaches its peak exhalation time, during which the airflow velocity attains its maximum value. It can be observed that vortices are generated at the lower lips of the chamber. This is mainly because water particles cannot enter the cylinder chamber horizontally along the wave propagation direction but need to inflate around the edge of the air chamber. At the same time, the PTO damping restricts the motion of the free surface, leading to localized water compression below the orifice. This creates inconsistencies in the velocity and direction of water movement at various locations, resulting in the formation of vortices at both the front and back lips, which also causes energy dissipation.

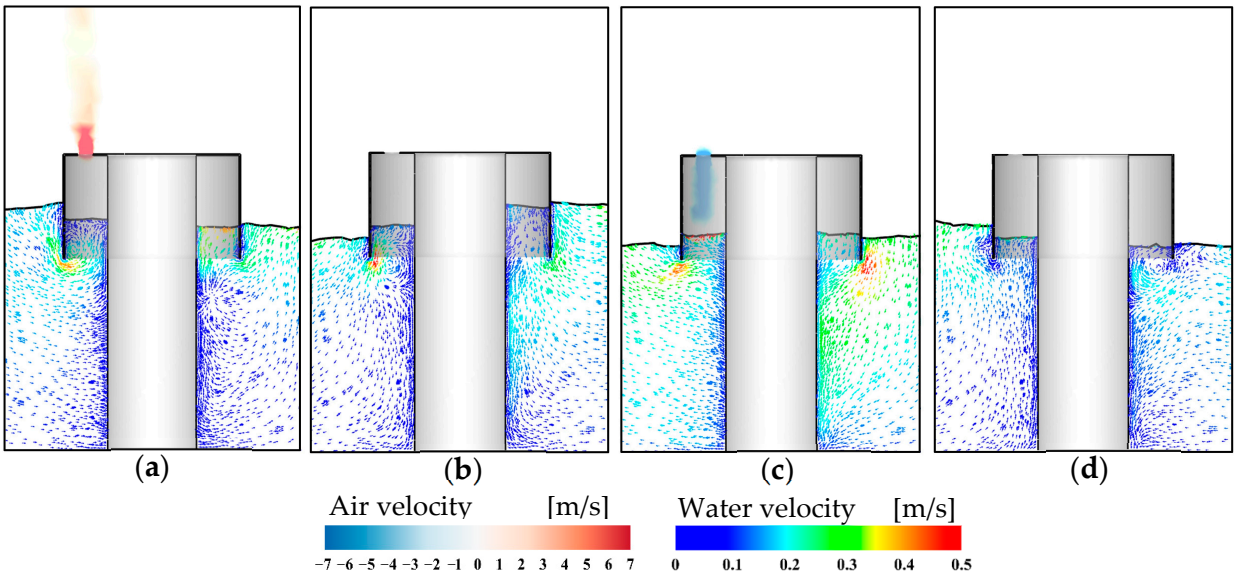

Figure 7. Distribution of flow characteristics in a wave cycle (H = 0.1 m, λ/l_1 = 12.0, and l_2/l_1 = 2.0). (**a**) $t = T/4$; (**b**) $t = 2T/4$; (**c**) $t = 3T/4$; (**d**) $t = T$.

At the moment of $2T/4$ in Figure 7b, the airflow velocity is close to zero as the device is transitioning from exhalation to inhalation. The free surface elevation on the leeward side of the air chamber is higher than that on the windward side due to the disturbance effect of the monopile. The airflow velocity reaches its maximum value during the inhalation phase at $3T/4$, as shown in Figure 7c. The velocity of the water particles below the orifice increases significantly, with the high-velocity regions mainly distributed at the lower lips of the chamber and near the free surface. At the moment of T in Figure 7d, the device is in the transition phase from inhalation to exhalation, and the airflow velocity approaches

zero again. The free surface inside the chamber is at the lowest position, and the exchange of water with the external flow field is minimal. Consequently, both the intensity and the influence scope of the vortex are not significant.

The effects of the chamber diameter on the flow characteristics of the hybrid device are plotted in Figure 8. The typical moment of $t = T/4$ is presented. In general, as the OWC chamber diameter increases, the distribution range of the high-velocity region for water particles inside the air chamber expands, especially on the leeward side. Furthermore, the velocity of the particles at the lower lip of the chamber increases with the chamber diameter, enabling more water to enter the chamber. In addition, vortices are formed at the inlet of the chamber, and the influence range of the vortex increases as the diameter increases, leading to more energy dissipation.

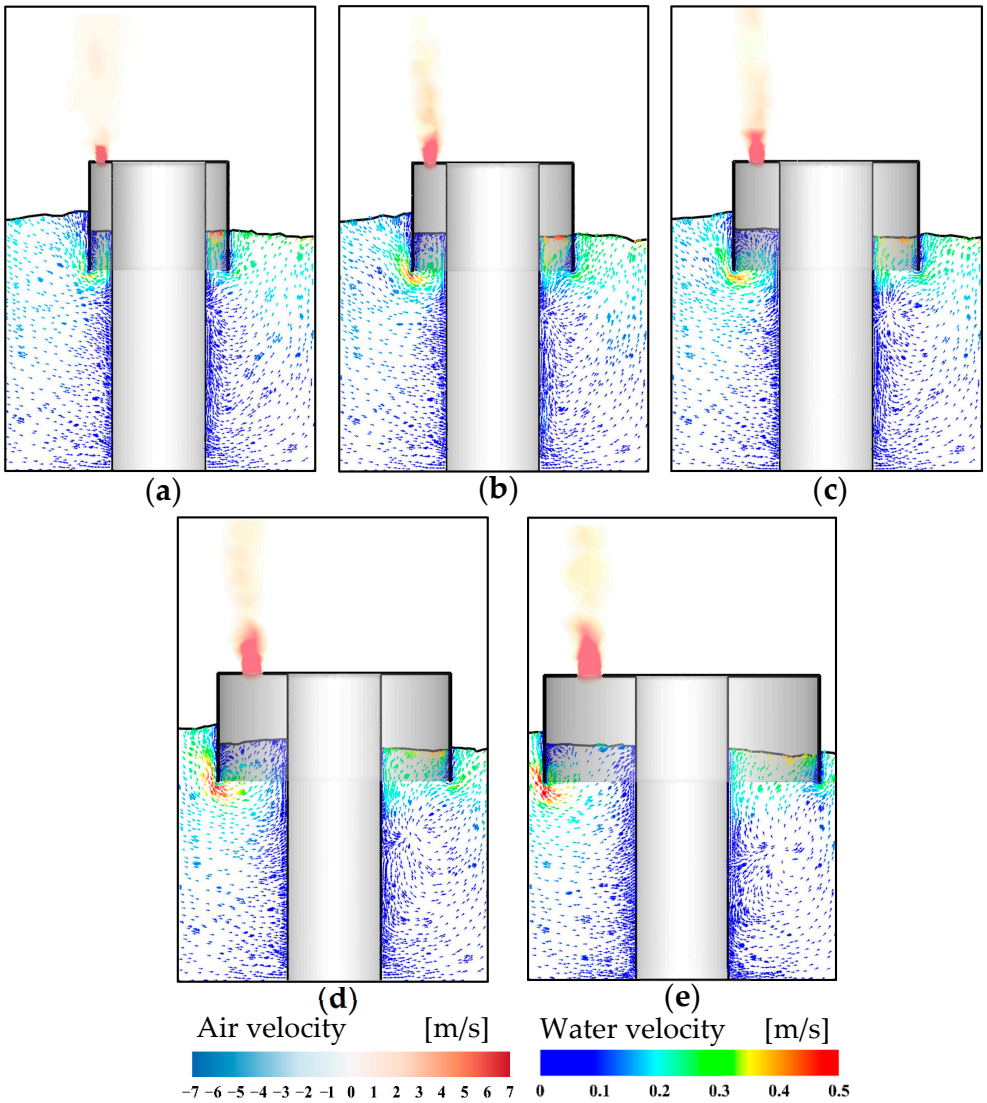

Figure 8. Effect of chamber diameter on flow characteristics at $t = T/4$ ($H = 0.1$ m and $\lambda/l_1 = 12.0$). (**a**) $l_2/l_1 = 1.5$; (**b**) $l_2/l_1 = 1.75$; (**c**) $l_2/l_1 = 2.0$; (**d**) $l_2/l_1 = 2.5$; (**e**) $l_2/l_1 = 3.0$.

Figure 9 shows the effect of the chamber diameter on the hydrodynamic performance of the hybrid OWC–wind device. Evidently, both the free surface elevation and air pressure decrease as the chamber diameter increases. This is attributed to the more intense free surface fluctuations inside the chamber at larger diameters, resulting in higher energy dissipation, as demonstrated in Figure 8. The *CWR* of the device is presented in Figure 9c. Although the free surface elevation and air pressure decrease with increasing diameter, the

OWC with a larger chamber has a greater free surface area, which enhances the airflow generated during the energy conversion process, ultimately leading to a higher *CWR*. The maximum *CWR* is observed at 0.466 when the relative diameter $l_2/l_1 = 0.3$.

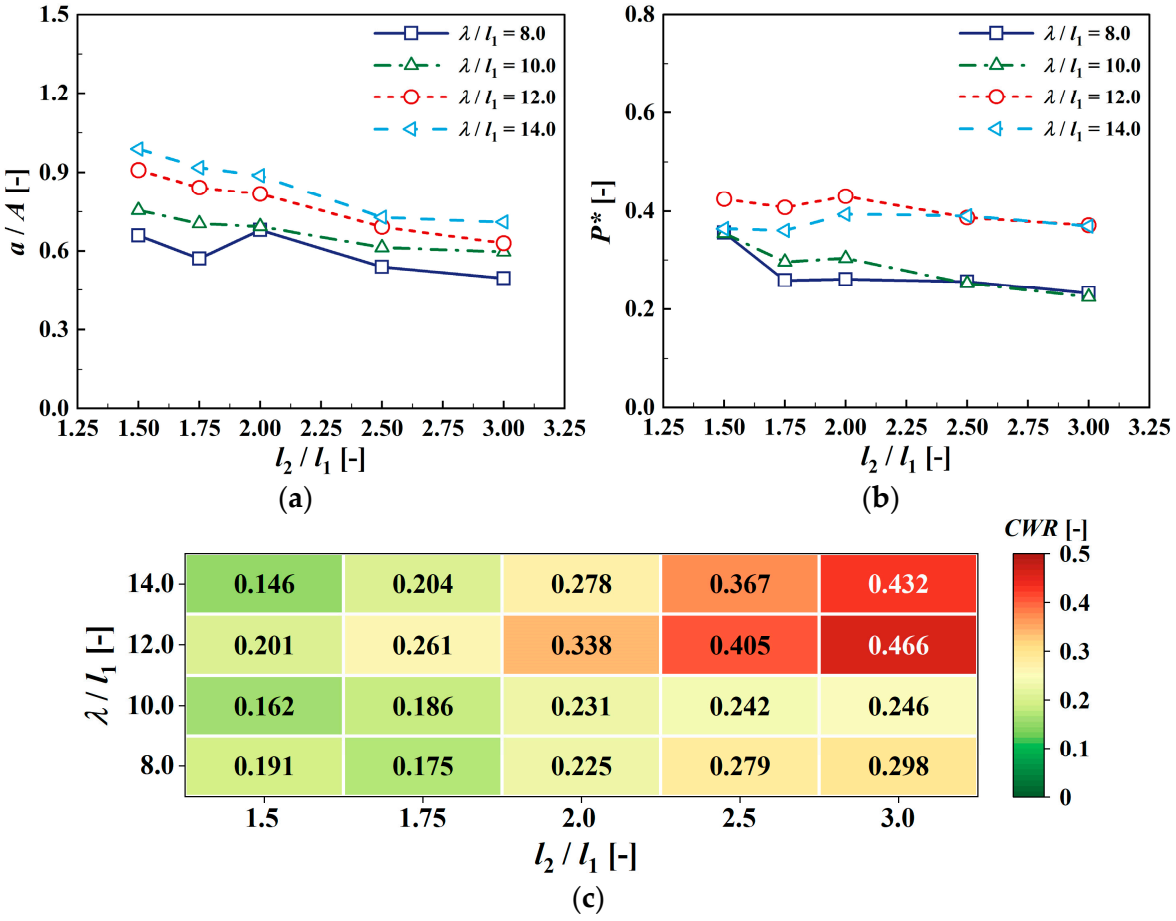

Figure 9. Effect of chamber diameter on hydrodynamic performance. (**a**) Relative amplitude of free surface elevation; (**b**) relative amplitude of air pressure; (**c**) capture width ratio.

The above results suggest that the hybrid OWC–wind device performs better with a larger chamber diameter. However, for practical applications, the diameter of the OWC device should also be determined based on the engineering requirements and the load capacity of the monopile. A larger-diameter OWC chamber may be selected as long as the safety conditions are met.

4.2. Effect of Chamber Draft

This section investigates the effects of the chamber draft on the hydrodynamic performance of the hybrid device. Five chamber drafts of d = 0.075 m, 0.1125 m, 0.15 m, 0.1875 m, and 0.225 m were selected, corresponding to relative chamber drafts of d/h = 0.1, 0.15, 0.2, 0.25, and 0.3, respectively. The chamber diameter of $l_2/l_1 = 3.0$ was chosen based on the results from the last section, and the dimensionless PTO damping was set to $\alpha = 1\%$.

Figure 10 illustrates the flow characteristics around the device under the influence of the chamber draft. Figure 10a indicates that, when the draft is small, waves can enter the chamber more easily and no significant vortices or energy loss occur at the lip of the chamber. However, a large difference in free surface elevation is observed around the monopile, with the free surface fluctuating more intensely, which negatively affects the energy capture of the device. As the draft increases, see Figure 10b–e, the waves are hindered from entering the chamber and vortices are formed at the front lip. Meanwhile,

the fluctuation of the free surface inside the chamber gradually decreases. Furthermore, since the wave energy is mainly concentrated at the surface, an excessively deep chamber is detrimental to wave energy capture.

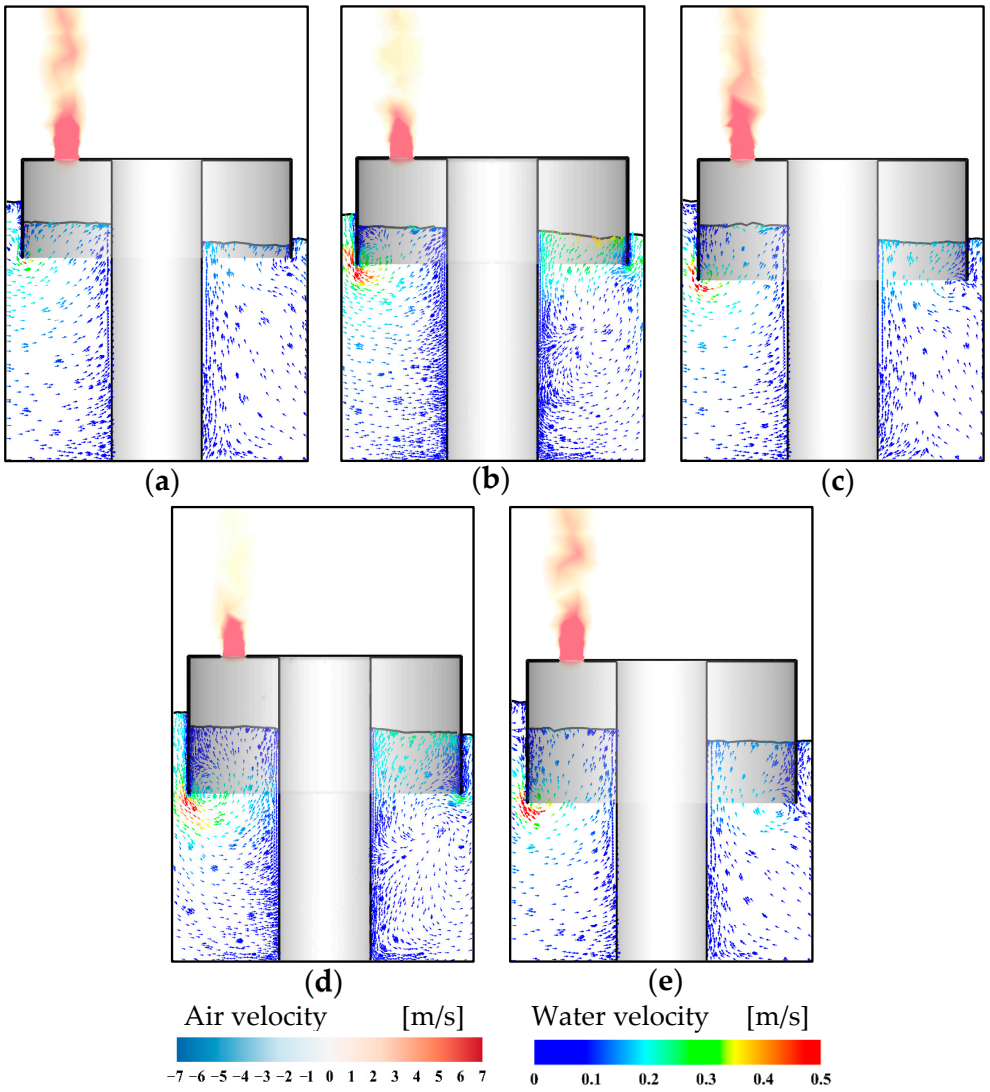

Figure 10. Effect of chamber draft on flow characteristics at $t = T/4$ (H = 0.1 m and λ/l_1 = 12.0). (**a**) d/h = 0.1; (**b**) d/h = 0.15; (**c**) d/h = 0.2; (**d**) d/h = 0.25; (**e**) d/h = 0.3.

The effect of the chamber draft on the hydrodynamic performance is presented in Figure 11. Generally, the free surface elevation decreases as the chamber draft increases because the waves are obstructed from entering the chamber at larger drafts, which is consistent with the trend observed in Figure 10. Regarding the air pressure, the amplitude values are closer under the two smaller-wave-length conditions. As the chamber draft increases, the air pressure rises and then decreases, with a sharp drop observed at the relative draft of d/h = 0.3. As for the CWR in Figure 11c, it can be concluded that the chamber draft has a significant impact on the performance of the hybrid device. An appropriate draft can effectively improve the energy capture performance of the device. When the relative draft d/h = 0.15, the OWC achieves the maximum CWR at 0.466. Additionally, the hybrid device is sensitive to the wave length, and the optimal performance is observed at a relative wave length of λ/l_1 = 12.0.

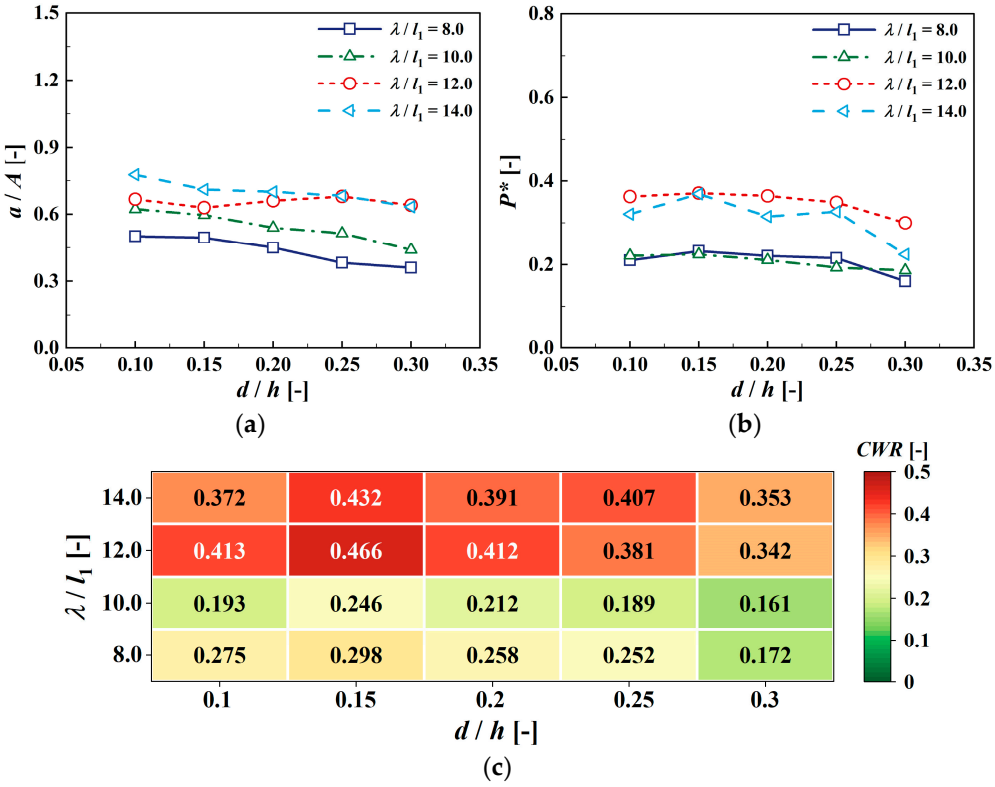

Figure 11. Effect of chamber draft on hydrodynamic performance. (**a**) Relative amplitude of free surface elevation; (**b**) relative amplitude of air pressure; (**c**) capture width ratio.

4.3. Effect of PTO Damping

In this section, the effects of PTO damping on energy capture performance are investigated. In the research models, the relative chamber diameter and the chamber draft were selected in terms of the above optimal studies, with l_2/l_1 = 3.0 and d/h = 0.15, respectively. The hybrid OWC–wind models equipped with five different PTO dampings were studied. The PTO damping is expressed by α, i.e., the ratio of the orifice opening area to the water column area, and α = 0.5%, 0.75%, 1.0%, 1.25%, and 1.5%, respectively.

Figure 12 presents the flow characteristics of the device under the effects of PTO dampings. Evidently, when the orifice opening is small (see Figure 12a,b), the free surface elevation inside the air chamber is lower due to the significant PTO damping, which restricts the oscillation of the water. At the same time, the free surface fluctuations become more pronounced with larger PTO damping. As the orifice opening increases, see Figure 12c–e, the damping effect diminishes and the velocity of the water particles inside the chamber increases, which leads to a higher free surface elevation. Additionally, in the case of small damping, the airflow is more easily expelled from the chamber.

Figure 13 shows the hydrodynamic performance of the hybrid device at different PTO damping levels. From Figure 13a,b, the PTO damping effect gradually decreases as the orifice opening increases, enabling the air inside the chamber to more easily exchange with the external environment, which leads to a decrease in the air pressure inside the chamber and consequently an increase in the free surface elevation. Since the air power is the product of the pressure and airflow rate and the variations in these two parameters with respect to PTO damping are opposite, there theoretically exists an optimal PTO damping that maximizes the air power. The CWR is shown in Figure 13c. Except for the relative incident wave length λ/l_1 = 14.0, the optimal CWR occurs at α = 0.75%, with a corresponding maximum value of 0.492.

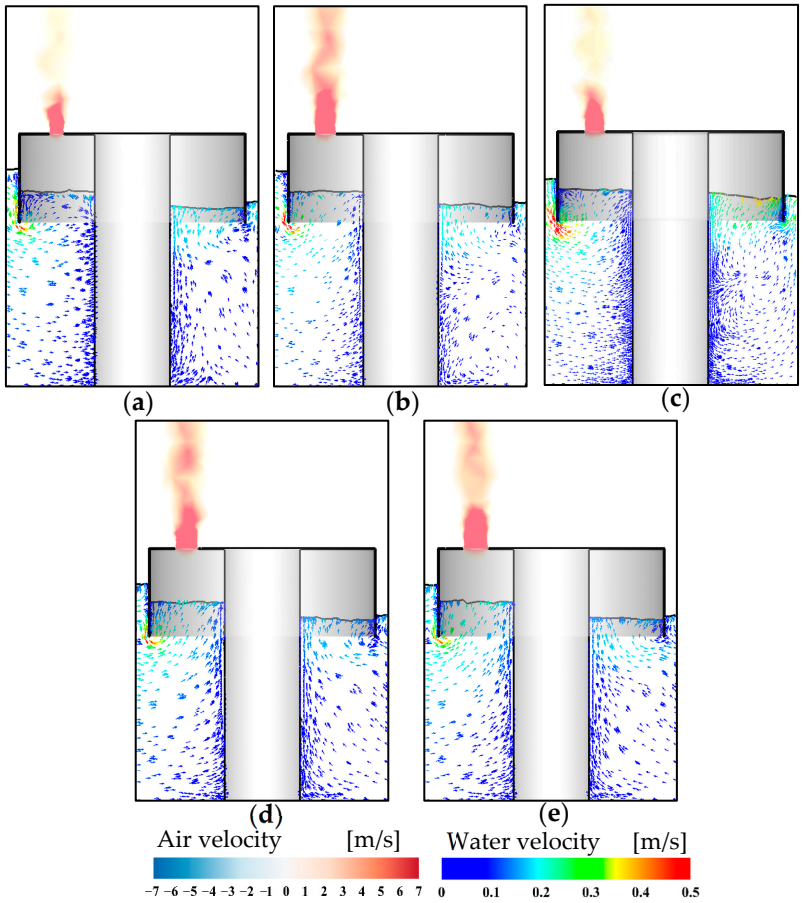

Figure 12. Effect of PTO damping on flow characteristics at $t = T/4$ (H = 0.1 m and λ/l_1 = 12.0). (**a**) α = 0.5%; (**b**) α = 0.75%; (**c**) α = 1.0%; (**d**) α = 1.25%; (**e**) α = 1.5%.

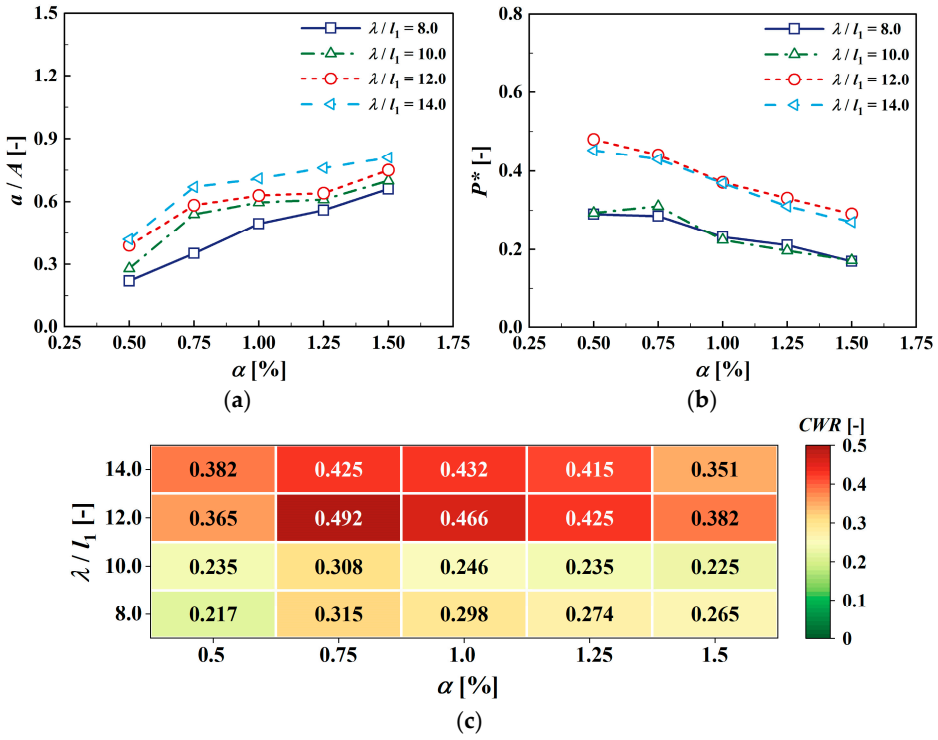

Figure 13. Effect of PTO damping on hydrodynamic performance. (**a**) Relative amplitude of free surface elevation; (**b**) relative amplitude of air pressure; (**c**) capture width ratio.

4.4. Performance Evaluation in Irregular Waves

To further evaluate the operating performance of the hybrid OWC–wind device under real sea states, irregular waves were employed for the calculations in this section. The device dimensions were selected according to the optimal values derived from the above results, i.e., a relative diameter l_2/l_1 = 3.0, a relative chamber draft d/h = 0.15, and an orifice opening ratio α = 0.75%. The irregular wave scenarios were generated based on the JONSWAP spectrum with the peak enhancement factor of γ = 3.3. A significant wave height of H_S = 0.1 m and five significant wave periods of T_S = 1.27 s, 1.45 s, 1.63 s, and 1.83 s were considered.

The flow characteristics and vortex development of the hybrid device at four typical instants in an irregular wave cycle are presented in Figure 14, with the case of H_S = 0.1 m and T_S = 1.83 s selected. The device reaches its exhalation peak at t = 44.84 s, as shown in Figure 14a. The free surface on the windward side remains relatively stable, while significant fluctuations occur on the leeward side due to the influence of the monopile. At this moment, vortices are observed at the entrance of the front wall. At t = 45.43 s in Figure 14b, the air velocity at the orifice is close to zero as the device enters the reversing phase. The flow characteristics are similar to those observed under regular wave conditions. In Figure 14c, the device reaches its inhalation peak and significant fluctuations in the free surface are observed on both the windward and leeward sides. In addition, the velocity of the water particles on the windward side increases significantly due to aerodynamic effects. At t = 46.45 s in Figure 14d, the air velocity returns to zero again, and the free surface elevation inside the chamber reaches its lowest position.

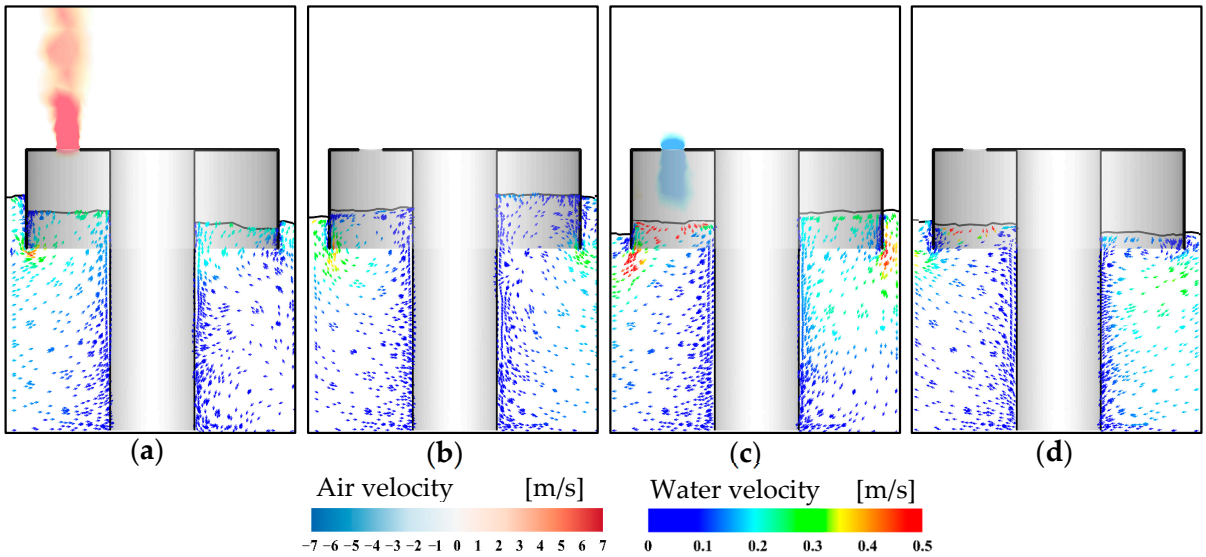

Figure 14. Distribution of flow characteristics in a wave cycle under irregular wave conditions (H_S = 0.1 m and T_S = 1.83 s). (**a**) t = 44.84 s; (**b**) t = 45.43 s; (**c**) t = 45.88 s; (**d**) t = 46.45 s.

The spectra of the free surface elevation and air pressure inside the chamber, obtained using the fast Fourier transform (FFT) method, are illustrated in Figure 15. The frequency-domain results of the spectral analysis were derived from the transformation of the time-domain data, i.e., the time series of the parameter in irregular waves. As shown in Figure 15a, both the spectral moment and peak of the free surface elevation increase with the significant period as more wave energy enters the air chamber during longer periods. Furthermore, a second-order spectral peak is observed when T_S = 1.27 s, which may be attributed to the more intense interaction between the waves and the device during shorter wave periods, leading to significant free surface fluctuations inside the chamber.

The air pressure spectrum is shown in Figure 15b, and the maximum spectral peak occurs at T_S = 1.63 s, indicating that the air pressure inside the chamber is higher at this condition.

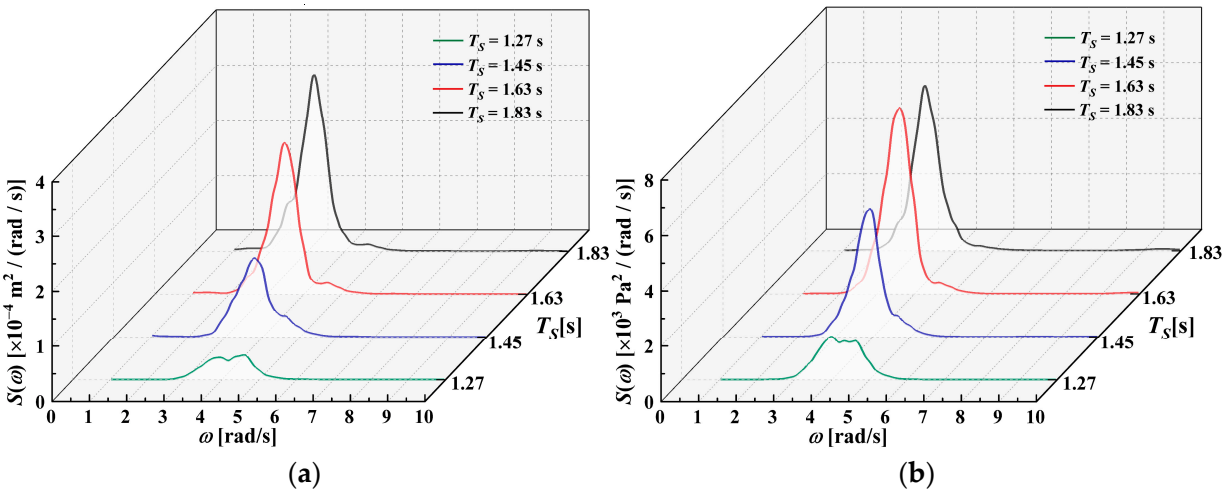

Figure 15. Spectral analysis of the irregular results. (**a**) Free surface elevation; (**b**) air pressure.

Figure 16 presents the pneumatic power output and the CWR of the hybrid device in irregular waves. Both the power output and CWR show a trend of first increasing and then decreasing with the significant wave period, reaching a peak at T_S = 1.63 s. The peak pneumatic power output and CWR are 3.07 W and 0.47, respectively. These results reveal that the hybrid device exhibits more pronounced resonance effects with the irregular wave scenario at the specific period. Therefore, the device could be optimally designed based on the dominant wave conditions to capture more wave energy.

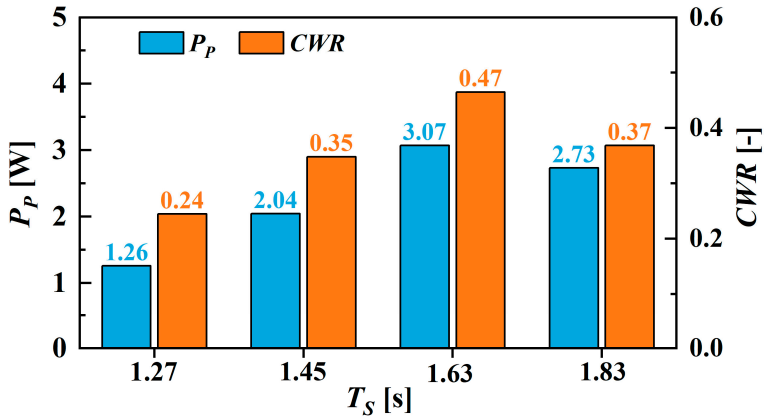

Figure 16. Power output and CWR in irregular waves.

5. Conclusions

In this paper, the hydrodynamic performance of a hybrid OWC–wind device was investigated. A CFD numerical model was established and validated by the corresponding experimental results. The flow characteristics and vortex development around the hybrid device were presented. The effects of geometrical parameters, such as chamber diameter, chamber draft, and PTO damping, on the energy capture performance were discussed. Variations in terms of free surface elevation, air pressure, and CWR were evaluated under both regular and irregular wave conditions.

The results indicate that the hybrid device performs better with a larger OWC chamber diameter. The velocity of the water particles at the front lip increases with the chamber diameter, leading to more intense fluctuations of the free surface, which result in higher

energy dissipation. The relative diameter is recommended to be $l_2/l_1 = 0.3$. Secondly, the chamber draft has a significant influence on the energy capture. When the draft is small, a large difference in free surface elevation is observed around the monopole. The hydrodynamic performance exhibits a trend of first increasing and then decreasing as the draft increases, with the optimal relative wave draft found at $d/h = 0.15$. The variations in free surface elevation and air pressure are oppositely influenced by PTO damping. When the PTO damping is too small, the airflow is restricted, leading to a decrease in energy capture. Conversely, when the PTO damping is too large, the air pressure inside the chamber becomes insufficient, resulting in lower performance. The peak CWR is observed with an orifice opening ratio of $\alpha = 0.75\%$. In addition, the hybrid device is sensitive to wave length. Under the optimal geometrical configurations, the device achieves a maximum CWR of 0.49 in regular waves and 0.47 in irregular waves.

This paper provides a foundational reference for the design of the hybrid OWC–wind device. However, the present study ignores the interactions between the air chamber and the air turbine. In future work, a numerical model that integrates the air chamber, a real air turbine, and a generator should be developed to enhance the wave-to-wire performance. Moreover, as ocean energy development extends to deeper seas, the hydrodynamic performance of wave energy devices integrated with floating wind turbines shall be further investigated.

Author Contributions: Conceptualization, C.X. and Z.L.; methodology, Z.L.; software, L.D.; validation, L.D. and Y.S.; formal analysis, L.D. and Y.S.; investigation, C.X. and Z.L.; resources, Z.L.; data curation, Y.S.; writing—original draft preparation, C.X.; writing—review and editing, L.D., Y.S. and Z.L.; visualization, C.X.; supervision, Z.L.; project administration, Z.L.; funding acquisition, Z.L. All authors have read and agreed to the published version of the manuscript.

Funding: This research was funded by the Shandong Provincial Major Basic Research Project of the Natural Science Foundation (Grant No. ZR2021ZD23); the National Natural Science Foundation of China (Grant Nos. 52471308 and 52301350); the Young top-notch talent project of the National Ten Thousand Talent Program; and the Program of Introducing Talents of Discipline to Universities (Grant No. B14028).

Institutional Review Board Statement: Not applicable.

Informed Consent Statement: Not applicable.

Data Availability Statement: The original contributions presented in this study are included in the article. Further inquiries can be directed to the corresponding author(s).

Conflicts of Interest: The authors declare no conflicts of interest.

References

1. Cui, L.; Zheng, S.; Zhang, Y.; Miles, J.; Iglesias, G. Wave Power Extraction from a Hybrid Oscillating Water Column-Oscillating Buoy Wave Energy Converter. *Renew. Sustain. Energy Rev.* **2021**, *135*, 110234. [CrossRef]
2. Guo, B.; Ringwood, J.V. Geometric Optimisation of Wave Energy Conversion Devices: A Survey. *Appl. Energy* **2021**, *297*, 117100. [CrossRef]
3. Doyle, S.; Aggidis, G.A. Development of Multi-Oscillating Water Columns as Wave Energy Converters. *Renew. Sustain. Energy Rev.* **2019**, *107*, 75–86. [CrossRef]
4. Falcão, A.F.O.; Henriques, J.C.C. Oscillating-Water-Column Wave Energy Converters and Air Turbines: A Review. *Renew. Energy* **2016**, *85*, 1391–1424. [CrossRef]
5. Li, H.; Shi, X.; Kong, W.; Kong, L.; Hu, Y.; Wu, X.; Pan, H.; Zhang, Z.; Pan, Y.; Yan, J. Advanced Wave Energy Conversion Technologies for Sustainable and Smart Sea: A Comprehensive Review. *Renew. Energy* **2025**, *238*, 121980. [CrossRef]
6. Elhanafi, A.; Kim, C.J. Experimental and Numerical Investigation on Wave Height and Power Take–off Damping Effects on the Hydrodynamic Performance of an Offshore–Stationary OWC Wave Energy Converter. *Renew. Energy* **2018**, *125*, 518–528. [CrossRef]

7. Kharati-Koopaee, M.; Fathi-Kelestani, A. Assessment of Oscillating Water Column Performance: Influence of Wave Steepness at Various Chamber Lengths and Bottom Slopes. *Renew. Energy* **2020**, *147*, 1595–1608. [CrossRef]
8. Yamaç, H.İ.; Koca, A. Shore Type Effect on Onshore Wave Energy Converter Performance. *Ocean Eng.* **2019**, *190*, 106494. [CrossRef]
9. Trivedi, K.; Ray, A.R.; Krishnan, P.A.; Koley, S.; Sahoo, T. Hydrodynamics of LIMPET Type OWC Device under Stokes Second-Order Waves. *Ocean Eng.* **2023**, *286*, 115605. [CrossRef]
10. He, F.; Lin, Y.; Pan, J.; Wei, M. Experimental Investigation of Vortex Evolution around Oscillating Water Column Wave Energy Converter Using Particle Image Velocimetry. *Phys. Fluids* **2023**, *35*, 015151. [CrossRef]
11. Mayon, R.; Ning, D.; Zhang, C.; Chen, L.; Wang, R. Wave Energy Capture by an Omnidirectional Point Sink Oscillating Water Column System. *Appl. Energy* **2021**, *304*, 117795. [CrossRef]
12. Wang, C.; Zhang, Y.; Deng, Z. Inclusion of a Pitching Mid-Wall for a Dual-Chamber Oscillating Water Column Wave Energy Converter Device. *Renew. Energy* **2022**, *185*, 1177–1191. [CrossRef]
13. M'zoughi, F.; Garrido, I.; Garrido, A.J.; De La Sen, M. Ann-Based Airflow Control for an Oscillating Water Column Using Surface Elevation Measurements. *Sensors* **2020**, *20*, 1352. [CrossRef] [PubMed]
14. Liu, Z.; McGregor, C.; Ding, S.; Wang, X. Study of a Three-Dimensional Model Simulation of a Speed Amplified Flux Switching Linear Generator for Wave Energy Conversion and Its Design Optimization in the Ocean Environment. *Energy* **2023**, *284*, 128625. [CrossRef]
15. Kim, J.S.; Nam, B.W.; Kim, S.; Park, J.; Park, S.; Kim, K.H. Experimental Study on Hydrodynamic Behavior and Energy Conversion of Multiple Oscillating-Water-Column Chamber in Regular Waves. *Ocean Eng.* **2023**, *280*, 114495. [CrossRef]
16. Wang, C.; Xu, H.; Zhang, Y.; Chen, W. Power Capture Analysis of a Five-Unit Oscillating Water Column Array Integrated into a Breakwater in Terms of Flow Field Visualization. *Energy Convers. Manag.* **2023**, *293*, 117449. [CrossRef]
17. Mustapa, M.A.; Yaakob, O.B.; Ahmed, Y.M.; Rheem, C.K.; Koh, K.K.; Adnan, F.A. Wave Energy Device and Breakwater Integration: A Review. *Renew. Sustain. Energy Rev.* **2017**, *77*, 43–58. [CrossRef]
18. Vicinanza, D.; Lauro, E.D.; Contestabile, P.; Gisonni, C.; Lara, J.L.; Losada, I.J. Review of Innovative Harbor Breakwaters for Wave-Energy Conversion. *J. Waterw. Port Coast. Ocean Eng.* **2019**, *145*, 03119001. [CrossRef]
19. Naty, S.; Viviano, A.; Foti, E. Wave Energy Exploitation System Integrated in the Coastal Structure of a Mediterranean Port. *Sustainability* **2016**, *8*, 1342. [CrossRef]
20. Neves, L.; Samadov, Z.; Lauro, E.D.; Delecluyse, K.; Haerens, P. The Integration of a Hybrid Wave Energy Converter in Port Breakwaters. In Proceedings of the 13th European Wave and Tidal Energy Conference, Naples, Italy, 1–6 September 2019; pp. 1–10.
21. Xu, C.; Huang, Z. A Dual-Functional Wave-Power Plant for Wave-Energy Extraction and Shore Protection: A Wave-Flume Study. *Appl. Energy* **2018**, *229*, 963–976. [CrossRef]
22. Howe, D.; Nader, J.R. OWC WEC Integrated within a Breakwater versus Isolated: Experimental and Numerical Theoretical Study. *Int. J. Mar. Energy* **2017**, *20*, 165–182. [CrossRef]
23. John Ashlin, S.; Sannasiraj, S.A.; Sundar, V. Performance of an Array of Oscillating Water Column Devices Integrated with an Offshore Detached Breakwater. *Ocean Eng.* **2018**, *163*, 518–532. [CrossRef]
24. Zhao, X.; Zhang, L.; Li, M.; Johanning, L. Experimental Investigation on the Hydrodynamic Performance of a Multi-Chamber OWC-Breakwater. *Renew. Sustain. Energy Rev.* **2021**, *150*, 111512. [CrossRef]
25. Zheng, S.; Zhang, Y.; Iglesias, G. Coast/Breakwater-Integrated OWC: A Theoretical Model. *Mar. Struct.* **2019**, *66*, 121–135. [CrossRef]
26. Zheng, S.; Antonini, A.; Zhang, Y.; Greaves, D.; Miles, J.; Iglesias, G. Wave Power Extraction from Multiple Oscillating Water Columns along a Straight Coast. *J. Fluid Mech.* **2019**, *878*, 445–480. [CrossRef]
27. Vipin, V.; Trivedi, K.; Koley, S. Optimization of Parameters of the OWC Wave Energy Converter Device Using MLP and XGBoost Models. *Results Phys.* **2023**, *55*, 107163. [CrossRef]
28. Cheng, Y.; Fu, L.; Dai, S.; Collu, M.; Ji, C.; Yuan, Z.; Incecik, A. Experimental and Numerical Investigation of WEC-Type Floating Breakwaters: A Single-Pontoon Oscillating Buoy and a Dual-Pontoon Oscillating Water Column. *Coast. Eng.* **2022**, *177*, 104188. [CrossRef]
29. Howe, D.; Nader, J.R.; Macfarlane, G. Experimental Investigation of Multiple Oscillating Water Column Wave Energy Converters Integrated in a Floating Breakwater: Wave Attenuation and Motion Characteristics. *Appl. Ocean Res.* **2020**, *99*, 102160. [CrossRef]
30. Wan, L.; Moan, T.; Gao, Z.; Shi, W. A Review on the Technical Development of Combined Wind and Wave Energy Conversion Systems. *Energy* **2024**, *294*, 130885. [CrossRef]
31. Sarmiento, J.; Iturrioz, A.; Ayllón, V.; Guanche, R.; Losada, I.J. Experimental Modelling of a Multi-Use Floating Platform for Wave and Wind Energy Harvesting. *Ocean Eng.* **2019**, *173*, 761–773. [CrossRef]
32. Abbaspour, M.; Farshforoush, A. Enhancing Wave Energy Harvesting through Integration of IEA 15 MW Wind Turbine on Oscillating Water Columns Equipped Platform. *Ocean Eng.* **2025**, *317*, 120069. [CrossRef]

33. Lee, H.H.; Chen, G.F.; Hsieh, H.Y. Study on an Oscillating Water Column Wave Power Converter Installed in an Offshore Jacket Foundation for Wind-Turbine System Part i: Open Sea Wave Energy Converting Efficiency. *J. Mar. Sci. Eng.* **2021**, *9*, 133. [CrossRef]
34. Michele, S.; Renzi, E.; Perez-Collazo, C.; Greaves, D.; Iglesias, G. Power Extraction in Regular and Random Waves from an OWC in Hybrid Wind-Wave Energy Systems. *Ocean Eng.* **2019**, *191*, 106519. [CrossRef]
35. Zhou, Y.; Ning, D.; Shi, W.; Johanning, L.; Liang, D. Hydrodynamic Investigation on an OWC Wave Energy Converter Integrated into an Offshore Wind Turbine Monopile. *Coast. Eng.* **2020**, *162*, 103731. [CrossRef]
36. Cong, P.; Teng, B.; Bai, W.; Ning, D.; Liu, Y. Wave Power Absorption by an Oscillating Water Column (OWC) Device of Annular Cross-Section in a Combined Wind-Wave Energy System. *Appl. Ocean Res.* **2021**, *107*, 102499. [CrossRef]
37. Liu, Z.; Xu, C.; Kim, K.; Choi, J.; Hyun, B. An Integrated Numerical Model for the Chamber-Turbine System of an Oscillating Water Column Wave Energy Converter. *Renew. Sustain. Energy Rev.* **2021**, *149*, 111350. [CrossRef]
38. López, I.; Pereiras, B.; Castro, F.; Iglesias, G. Optimisation of Turbine-Induced Damping for an OWC Wave Energy Converter Using a RANS-VOF Numerical Model. *Appl. Energy* **2014**, *127*, 105–114. [CrossRef]
39. Yakhot, V.; Orszag, S.A. Renormalization Group Analysis of Turbulence. I. Basic Theory. *J. Sci. Comput.* **1986**, *1*, 3–51. [CrossRef]
40. Liu, Z.; Xu, C.; Kim, K. A CFD-Based Wave-to-Wire Model for the Oscillating Water Column Wave Energy Convertor. *Ocean Eng.* **2022**, *248*, 110842. [CrossRef]